The Astrophysical Journal, 961:37 (9pp), 2024 January 20 https://doi.org/10.3847/1538-4357/ad02f8

Disappearing Galaxies: The Orientation Dependence of JWST-bright, HST-dark, Star-forming Galaxy Selection

R. K. Cochrane[1,2], D. Anglés-Alcázar[2,3], F. Cullen[4], and C. C. Hayward[2]
[1] Department of Astronomy, Columbia University, New York, NY 10027, USA; rc3660@columbia.edu
[2] Center for Computational Astrophysics, Flatiron Institute, 162 Fifth Avenue, New York, NY 10010, USA
[3] Department of Physics, University of Connecticut, 196 Auditorium Road, U-3046, Storrs, CT 06269-3046, USA
[4] Institute for Astronomy, University of Edinburgh, Royal Observatory, Blackford Hill, Edinburgh, EH9 3HJ, UK
Received 2023 June 24; revised 2023 October 11; accepted 2023 October 11; published 2024 January 11

Abstract

Galaxies that are invisible in deep optical–near-infrared imaging but detected at longer wavelengths have been the focus of several recent observational studies, with speculation that they could constitute a substantial missing population and even dominate the cosmic star formation rate density at $z \gtrsim 4$. The depths now achievable with JWST at the longest wavelengths probed by the Hubble Space Telescope (HST), coupled with the transformative resolution at longer wavelengths, are already enabling detailed, spatially resolved characterization of sources that were invisible to HST, often known as "HST-dark" galaxies. However, until now, there has been little theoretical work to compare against. We present the first simulation-based study of this population, using highly resolved galaxies from the Feedback in Realistic Environments project, with multiwavelength images along several lines of sight forward-modeled using radiative transfer. We naturally recover a population of modeled sources that meet commonly used selection criteria ($H_{\rm AB} > 27$ mag and $H_{\rm AB} - {\rm F444W} > 2.3$). These simulated HST-dark galaxies lie at high redshifts ($z = 4$–7), have high levels of dust attenuation ($A_V = 2$–4), and display compact recent star formation ($R_{1/2,4.4\,\mu{\rm m}} \lesssim 1$ kpc). Orientation is very important: for all but one of the 17 simulated galaxy snapshots with HST-dark sight lines, there exist other sight lines that do not meet the criteria. This result has important implications for comparisons between observations and models that do not resolve the detailed star-dust geometry, such as semianalytic models or coarsely resolved hydrodynamical simulations. Critically, we demonstrate that HST-dark sources are not an unexpected or exotic population, but a subset of high-redshift, highly dust-attenuated sources viewed along certain lines of sight.

Unified Astronomy Thesaurus concepts: Galaxy evolution (594); High-redshift galaxies (734); Radiative transfer simulations (1967)

1. Introduction

It has been known for decades that not all bright submillimeter galaxies (SMGs) have detectable optical–near-infrared (OIR) counterparts (Lilly et al. 1999; Smail et al. 1999, 2000, 2002a, 2004; Bertoldi et al. 2000; Frayer et al. 2000, 2004; Dannerbauer et al. 2002; Wang et al. 2007). This can hamper redshift determination; indeed, the brightest source in the Hubble Deep Field at 850 μm, HDF850.1, showed no clear OIR counterpart (Hughes et al. 1998; Cowie et al. 2009), and it took over a decade for its redshift to be identified ($z = 5.183$; Walter et al. 2012).

Other populations of OIR-dark galaxies have been selected using optical–infrared colors. Galaxies first identified by red $R - K$ colors and faint K-band fluxes were called "extremely red objects" (EROs; Elston et al. 1988; Hu & Ridgway 1994); some, but not all, of these sources were also identified in the submillimeter (Cimatti et al. 1998; Dey et al. 1999). Later, Spitzer-IRAC imaging (Fazio et al. 2004) enabled efficient surveys of new red populations (Wilson et al. 2004; Huang et al. 2011) and better separation of passive and star-forming galaxies. Wang et al. (2016) introduced a color selection to identify massive, high-redshift galaxies using a combination of deep Hubble Space Telescope (HST) H-band imaging and IRAC CH2: $H_{\rm AB} - [4.5] > 2.25$ mag. Of the sources selected in this way, 62% were detected down to $S_{870\,\mu{\rm m}} > 0.6$ mJy (Wang et al. 2019). OIR-faint sources have also been detected at radio wavelengths (Kondapally et al. 2021; Talia et al. 2021; Enia et al. 2022; van der Vlugt et al. 2022; Behiri et al. 2023).

OIR-faint galaxies are important for several reasons. First, several works have suggested that they may contribute significantly to the cosmic star formation rate density (SFRD) at $z \gtrsim 3$, though estimates of the contribution vary (e.g., Wang et al. 2016 calculated that H-dark sources contribute 15%–25% of the SFRD at $z = 4$–5, while Sun et al. 2021 estimated 8^{+8}_{-4}% at $z = 3$–5; see also Williams et al. 2019; Yamaguchi et al. 2019; Xiao et al. 2023). Hence, excluding OIR-faint sources from censuses of star formation (e.g., by using H- or K-selected samples, or by requiring OIR counterparts for sources selected in other ways) will lead to a redshift-dependent underestimate of the SFRD. Second, degeneracies between the signatures of redshift, age, and dust attenuation in photometry result in the possibility of dusty sources contaminating surveys of high-redshift quiescent galaxies (e.g., Smail et al. 2002b; Dunlop et al. 2007; Simpson et al. 2017b). Third, OIR-faint sources may help constrain theoretical models of galaxy formation and evolution. Wang et al. (2019) showed that the number density of $H_{\rm AB} > 27$ mag sources predicted by an early version of the L-GALAXIES semianalytic model (SAM; Henriques et al. 2015) lies ∼2 orders of magnitude below the observed number density. They speculated that our understanding of massive-galaxy formation may require substantial revision.

The advent of the Atacama Large Millimeter/submillimeter Array (ALMA) has facilitated statistical studies of large samples of submillimeter-bright galaxies, including locating and resolving sources identified with single-dish telescopes (e.g., Hodge et al. 2013; Karim et al. 2013; Simpson et al. 2014, 2015, 2020; Stach et al. 2018). This has enabled more detailed exploration of the number density and physical properties of the subset of submillimeter-bright galaxies that are also OIR-dark. Using ALMA follow-up of SCUBA-2-identified sources within the UKIDSS Ultra Deep Survey (Simpson et al. 2017a; Stach et al. 2018, 2019; Dudzevičiūtė et al. 2020), Smail et al. (2021) found that $15\% \pm 2\%$ of the bright ($S_{850\,\mu\mathrm{m}} > 3.6$ mJy) SMG population is fainter than $K_{\mathrm{AB}} = 25.3$ mag. These K-faint galaxies tend to have higher redshifts and dust attenuation than their K-detected counterparts (see also the high photometric redshifts derived for the HST-dark, 1.1 mm–selected sources from Franco et al. 2018, and for OIR-dark galaxies selected at longer wavelengths from Williams et al. 2019; Casey et al. 2021; Manning et al. 2022). However, given the relatively low angular resolution of IRAC (FWHM $\sim 2''$) and the typically small angular sizes of OIR-dark sources, characterizing the spatial distribution of rest-frame optical emission was not possible until the launch of JWST.

JWST has provided the sensitivity and wavelength coverage required to gather high angular resolution (compared to IRAC), multiwavelength imaging, and hence constrain the properties of sources that were invisible to HST (e.g., Fujimoto et al. 2023; Gómez-Guijarro et al. 2023; Pérez-González et al. 2023; Rodighiero et al. 2023; Smail et al. 2023). Employing a similar selection used in previous studies to identify dusty galaxies at $z = 3$–6 ($H_{\mathrm{AB}} > 27$ and $H_{\mathrm{AB}} - \mathrm{F444W}_{\mathrm{AB}} > 2.0$; e.g., Caputi et al. 2012; Wang et al. 2016), Barrufet et al. (2023) selected a sample of 30 HST-dark sources within CEERS NIRCam imaging (Finkelstein et al. 2022). They showed that galaxies selected using these criteria tend to be fairly dust-obscured ($A_V \sim 2$), massive ($M_\star \sim 10^9$–$10^{10.5}\,M_\odot$) star-forming galaxies at $z \sim 2$–8 that lie approximately along the main sequence. Using the same data, Nelson et al. (2023) identified a population of spatially extended ($R_{e,4.4\,\mu\mathrm{m}} > 0.''17$), 4.4 μm–bright, H-faint sources, with higher inferred stellar masses, the majority in the range $M_\star = 10^{10-11}\,M_\odot$ (using EAzY, the median stellar mass is $M_\star = 10^{10.5}\,M_\odot$, but they also find systematic differences between spectral energy distribution (SED) fitting codes). These 4.4 μm-identified sources appear to have lower stellar masses, on average, than submillimeter-identified OIR-dark sources. For example, the median stellar masses of the K-faint and whole sample of Smail et al. (2021) are $M_\star = 10^{11.10\pm0.04}\,M_\odot$ and $M_\star = 10^{11.00\pm0.06}\,M_\odot$, respectively, and some of the most extreme submillimeter-bright sources are likely even more massive (e.g., the stellar mass derived for the $S_{850\,\mu\mathrm{m}} = 15.3 \pm 0.4$ mJy, $z = 4.26$ source presented by Smail et al. 2023 is $10^{11.8}\,M_\odot$).

Despite substantial observational interest in HST-dark galaxies, until now there have been no focused theoretical studies on the nature of HST-dark galaxies. In this paper, we study the physical properties of galaxies modeled with highly resolved zoom-in simulations using the Feedback in Realistic Environments (FIRE; Hopkins et al. 2014, 2018, 2023) model that meet observational HST-dark selection criteria. In Section 2, we describe the simulations and the radiative transfer calculations performed to forward-model observable emission. We describe the selection of HST-dark galaxies. In Section 3, we study the demographics, dust attenuation properties, and sizes of our simulated HST-dark galaxies, and highlight a substantial line-of-sight dependence of the source section. We draw our conclusions in Section 4.

2. Simulations and HST-dark Source Selection

2.1. FIRE Simulations

The FIRE[5] project is a suite of state-of-the-art hydrodynamical cosmological zoom-in simulations described fully in Hopkins et al. (2014, FIRE-1), Hopkins et al. (2018, FIRE-2), and Hopkins et al. (2023, FIRE-3). In this paper, we study galaxies modeled with FIRE-2, which uses the "meshless finite mass" mode of the N-body+hydrodynamics code GIZMO[6] (Hopkins 2015); gravitational forces are computed following the methods presented in Hopkins et al. (2013), using an improved version of the parallel TreeSPH code GADGET-3 (Springel et al. 2005). Cooling and heating processes including free–free, photoionization/recombination, Compton, photoelectric, metal-line, molecular, and fine-structure processes are modeled from $T = 10$ K to $T = 10^{10}$ K. Star particles form from locally self-gravitating, molecular, Jeans unstable gas above a minimum hydrogen number density $n_{\mathrm{H}} \geqslant 1000\,\mathrm{cm}^{-3}$. Each star particle represents a single stellar population with known mass, age, and metallicity, injecting feedback locally in the form of mass, momentum, energy, and metals from Type Ia and Type II supernovae, stellar winds, photoionization and photoelectric heating, and radiation pressure, with all feedback quantities and their time dependence taken directly from the STARBURST99 population synthesis model (Leitherer et al. 1999).

We study the central galaxies of eight massive halos originally selected and simulated by Feldmann et al. (2016, 2017) as part of the MASSIVEFIRE-1 suite. The same halos were studied in Cochrane et al. (2022) and Cochrane et al. (2023b). The first four halos are drawn from the "A-series" (A1, A2, A4, and A8); these halos were selected to have dark matter halo masses of $M_{\mathrm{halo}} \sim 10^{12.5}\,M_\odot$ at $z = 2$. The "A-series" halos studied in this paper are drawn from Anglés-Alcázar et al. (2017), who resimulated them down to $z = 1$ with the upgraded FIRE-2 physics model (Hopkins et al. 2018). We supplement these halos by rerunning four more halos from Feldmann et al. (2017), with the updated FIRE-2 physics. Two of the halos are drawn from their "B-series" (B1 and B2) and two from the "C-series" (Cm1:0, hereafter C1, and C2:0, hereafter C2). Halos B2, C1, and C2 tend to be more massive than the A-series halos. The mass resolution for both gas and star particles is $3.3 \times 10^4\,M_\odot$, $2.7 \times 10^5\,M_\odot$, and $2.2 \times 10^6\,M_\odot$, for A-, B-, and C-series halos, respectively. For dark matter particles, the respective mass resolutions are $1.7 \times 10^5\,M_\odot$, $1.4 \times 10^6\,M_\odot$, and $1.1 \times 10^7\,M_\odot$. Convergence tests for these simulations are presented in Cochrane et al. (2022, see Appendix B).

2.2. Modeling Observable Emission

We model SEDs and multiwavelength emission maps at every snapshot, between $z \sim 8$ and $z \sim 1$, for each of the eight simulated halos (in total, 1736 snapshots). Following Cochrane et al. (2019, 2022, 2023a, 2023b) we use the SKIRT[7] radiative

[5] https://fire.northwestern.edu
[6] http://www.tapir.caltech.edu/~phopkins/Site/GIZMO.html
[7] http://www.skirt.ugent.be

transfer code (version 8; Baes et al. 2011; Camps & Baes 2015) to make predictions for emission between rest-frame ultraviolet (UV) and far-infrared (FIR) wavelengths along seven lines of sight. For all snapshots, gas and star particles within $0.1R_{\rm vir}$ are drawn directly from FIRE-2 simulation data. Dust particles are assumed to follow the distribution of the gas particles, with a dust-to-metal mass ratio of 0.4 (Dwek 1998; James et al. 2002). This is a reasonable assumption for enriched, massive galaxies like these. We have checked that using the metallicity-dependent dust-to-metal ratios drawn from the relations derived by Rémy-Ruyer et al. (2014) would yield similar values. We assume dust destruction at $>10^6$ K (Draine & Salpeter 1979; Tielens et al. 1994). Following Cochrane et al. (2019, 2022, 2023a, 2023b), we model a mixture of graphite, silicate, and polycyclic aromatic hydrocarbon grains using the Weingartner & Draine (2001) Milky Way dust prescription. Star particles are assigned Bruzual & Charlot (2003) SEDs based on their ages and metallicities. We perform the radiative transfer on an octree dust grid, in which cell sizes are adjusted according to the dust density distribution, with the condition that no dust cell may contain more than 0.0001% of the total dust mass of the galaxy. SKIRT parameter convergence tests are presented in Cochrane et al. (2022).

The output from SKIRT comprises predictions for global galaxy SEDs as well as maps of the resolved emission at each of the ∼100 wavelengths modeled, for seven lines of sight. We transform flux densities in Jy to AB magnitudes (using a zero-point of 3631 Jy).

2.3. HST-dark Source Selection

Following selection criteria similar to those employed by Wang et al. (2016) and Barrufet et al. (2023), we select sight lines from our snapshots that meet the following H-band and color criteria:

$$H_{\rm AB} > 27 \text{ mag} \quad (1)$$

and

$$H_{\rm AB} - {\rm F444W}_{\rm AB} > 2.3. \quad (2)$$

Variations in both H-band magnitude and color with orientation result in snapshots for which some lines of sight meet the criteria and some do not. We define two subsets of lines of sight of the HST-dark subsample: "selected" are orientations that meet the criteria; "not-selected" are orientations that do not meet the criteria, where there exist other orientations of the same snapshot (i.e., the same galaxy and redshift) that do meet the criteria. In total, we obtain 17 independent galaxy snapshots that meet the selection criteria at one or more viewing angles. We simulate a total of 119 viewing angles of these sometimes-HST-dark snapshots, where 46 meet the selection and 73 do not. We study the viewing angle dependence in more detail in Section 3.5.

In Figure 1, we show the positions in the color–magnitude plane of selected and not-selected lines of sight of snapshots that are classified as HST-dark from one or more viewing angles. In gray, we show all seven lines of sight of FIRE snapshots with no HST-dark sight lines. The selected HST-dark subsample occupies a similar region of this parameter space to the observed sample of Barrufet et al. (2023), giving confidence in the realism of our simulated galaxies. Lines of sight in the not-selected sample tend to lie just outside the boundaries of the selection, either because they are slightly too bright at 1.6 μm, slightly too blue, or both. Only one simulated galaxy snapshot is HST-dark from all seven modeled viewing angles. This implies that HST-dark sources selected in this way are not an entirely unique population; instead, they are sources viewed from preferential orientations that would be visible by HST if viewed from other directions. In Section 3, we explore the physical properties of the selected HST-dark sources and the drivers of this orientation dependence.

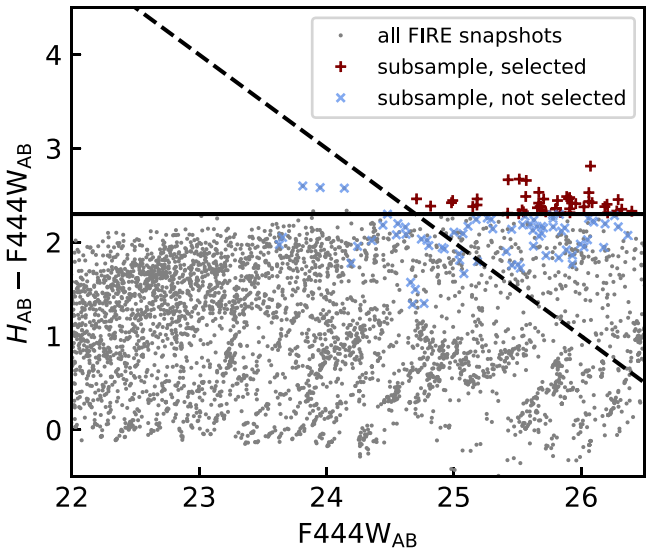

Figure 1. Selection of snapshot orientations detected as HST-dark (dark red), according to the criteria: $H_{\rm AB} - {\rm F444W}_{\rm AB} > 2.3$ (solid line) and $H_{\rm AB} > 27$ mag (dashed line). Lines of sight that do not meet this criteria, when one or more lines of sight of the same galaxy snapshot do, are plotted in blue. These tend to be slightly too blue, slightly too H-bright, or both. Lines of sight for snapshots with no orientations meeting the criteria are plotted in gray.

2.4. Comments on Selection Criteria

Here, we comment on the effects of each of the selection criteria on the demographics of the selected population. The H-dark criterion favors the selection of higher-redshift sources, whereas the color criterion favors intermediate redshifts. A looser color criterion (i.e., extending to bluer colors) would lead to the inclusion of higher-redshift H-faint sources into the sample. All of our selected snapshots lie within the redshift range $4 < z < 7$, but the redshift distribution and range will depend on the details of the mass assembly and metal enrichment of the simulated galaxies. While a modest-sized sample constructed in this way does not allow predictions for the redshift distribution of observed sources, we can note some general trends. First, the selection criteria identify simulated sources within the general redshift range of the HST-dark, IRAC/F444W-bright sources reported by observational studies (e.g., Wang et al. 2019; Barrufet et al. 2023; Nelson et al. 2023). The modeled 4.4 μm emission of our sources is fairly faint (F444W$_{\rm AB} \gtrsim 24.8$ mag) compared to observed HST-dark sources, but still within the range measured by Barrufet et al. (2023).

Importantly, the OIR-dark, submillimeter-bright population tends to extend to lower redshifts: the median photometric redshift of the K-dark SMGs studied by Smail et al. (2021) is $z = 3.44 \pm 0.06$, the majority lying in the range $z = 3$–4, with a handful below $z = 3$. Our simulated sources become too H-bright below $z \sim 4$, but we would expect that dustier, more submillimeter-bright sources would be more highly attenuated in the H band and hence meet the H-faint criterion (the

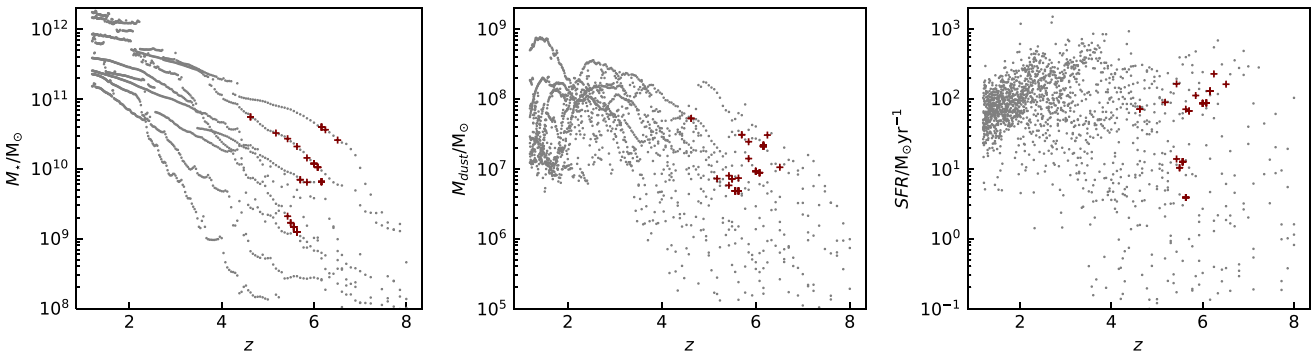

Figure 2. The redshift evolution of stellar mass (left), dust mass (middle), and star formation rate (right), for all eight FIRE halos in this study (gray). Snapshots with HST-dark sight lines are plotted in red. Simulated galaxies with HST-dark sight lines span redshifts ∼4–7, with a broad range of stellar masses (from $\sim 10^9\,M_\odot$ to $\sim 10^{11}\,M_\odot$).

degeneracy between A_V and z is also discussed in Caputi et al. 2012, Wang et al. 2016, and Sun et al. 2021). Due to the limited dynamic range of halos simulated here, we do not model these submillimeter-bright, highly attenuated sources. Instead, we focus on the submillimeter-faint ($S_{850\,\mu m} \lesssim 1$ mJy), HST-dark population.

Finally, we comment on some modeling choices that affect the predicted fluxes of our simulated galaxies, and therefore the selection. In this work, following the methods of Cochrane et al. (2019, 2022, 2023a, 2023b), we do not implement any models for unresolved, small-scale dust. Ma et al. (2019) argue that the FIRE galaxies are sufficiently well resolved that this is not necessary. Tests have, however, been performed using the MAPPINGS III models (Groves et al. 2008) to model emission from the warm dust associated with the unresolved birth clouds of young star clusters. Liang et al. (2021) studied the impact of varying two MAPPINGS parameters, $\log C$ (the H II region compactness) and $f_{\rm PDR}$ (the covering fraction of the associated photodissociation regions) on the predicted SED. They found that the choice of $\log C$ had little impact on the UV–optical SED, while a higher $f_{\rm PDR}$ yields a higher dust optical depth, and therefore reduced UV–optical fluxes and a steeper dust attenuation curve. Although the effects on the SED are modest, we note that implementing the MAPPINGS models with a nonzero $f_{\rm PDR}$ could result in more snapshots meeting the HST-dark criteria (due to both lower H-band fluxes and redder colors).

3. The Nature of HST-dark Sources

3.1. HST-dark Source Demographics

In Figure 2, we show the redshift evolution of stellar mass, dust mass, and star formation rate for the eight FIRE halos studied. We briefly summarize the demographics of snapshots with HST-dark lines of sight here. Stellar masses of the galaxies in selected snapshots range from $\sim 10^9\,M_\odot$ to $\sim 10^{11}\,M_\odot$, with mean $\log_{10}(M_*/M_\odot) = 9.8$. Dust masses range from $\sim 5\times 10^6\,M_\odot$ to $\sim 5\times 10^7\,M_\odot$, with mean $\log_{10}(M_{\rm dust}/M_\odot) = 7.0$. Star formation rates (defined here as instantaneous) range from a few to a few hundred solar masses per year, with mean $\mathrm{SFR} = 56\,M_\odot\,\mathrm{yr}^{-1}$. These are in broad agreement with the inferred physical properties of 4.4/4.5 μm-selected HST-dark sources (Sun et al. 2021; Barrufet et al. 2023; Nelson et al. 2023). In contrast, the submillimeter-selected K-dark galaxies studied by Smail et al. (2021) have higher derived dust masses ($>10^8\,M_\odot$), with stellar masses $\sim 10^{11}\,M_\odot$; the majority of those sources lie at $z < 4$.

3.2. Dust Attenuation of HST-dark Sources

By comparing intrinsic and attenuated emission as a function of wavelength, we can study the effective attenuation curves of the simulated galaxies at each snapshot. In Figure 3, we plot median dust attenuation A_λ (left) and median V-band-normalized dust attenuation A_λ/A_V (middle) versus wavelength, for the subsample of lines of sight selected as HST-dark and red (red line) and not-selected lines of sight of the same snapshots (blue line). For comparison, we also show curves generated using all snapshots in the redshift range within which our HST-dark-selected sources fall, $4 < z < 7$. It is clear from the left panel that both selected and not-selected lines of sight of the HST-dark snapshots are significantly more attenuated, on average, than other sources in the same redshift range. Once normalized by A_V, though, the shapes of the attenuation curves are very similar (middle panel) and grayer than the curve derived by Calzetti et al. (2000) (note, though, that we have used the same dust grain model for all simulated sources and snapshots: different choices of dust grain mix and size distributions would change the details of the attenuation and possibly also change the numbers of simulated sources that meet the HST-dark selection criteria). In the right panel, we show a histogram of A_V for the different populations. The median A_V values for selected and not-selected lines of sight of HST-dark snapshots are $A_V = 2.8$ and 2.6, respectively, while $A_V = 0.5$ for FIRE snapshots in the redshift range $z = 4-7$.

3.3. Physical and Light-based Sizes of HST-dark Sources

3.3.1. Physical Sizes of HST-dark Sources

In Figure 4(a), we present distributions of the half-mass, half-SFR, and half-dust mass sizes of galaxies with and without HST-dark sight lines. These sizes are calculated from particle data and are hence mass-weighted rather than light-weighted. The stellar mass (both of all stars and recently formed stars) is extremely compact for the HST-dark sources, with $R_{1/2,M_*}$ and $R_{1/2,\mathrm{SFR}_{10\,\mathrm{Myr}}} < 0.5$ kpc. Although more extended than the stellar mass distribution, the dust mass is also compact ($R_{1/2,M_{\rm dust}} \sim 1$ kpc). For the whole sample at $z = 4$–7, the median $R_{1/2,\mathrm{SFR}_{10\,\mathrm{Myr}}}/R_{1/2,M_{\rm dust}} = 0.49$. For the subsample of sources with one or more lines of sight meeting the HST-dark criteria, the median $R_{1/2,\mathrm{SFR}_{10\,\mathrm{Myr}}}/R_{1/2,M_{\rm dust}} = 0.14$, with median $R_{1/2,\mathrm{SFR}_{10\,\mathrm{Myr}}} = 0.12$ kpc. Thus, our simulated HST-dark sources feature particularly compact star formation embedded within a

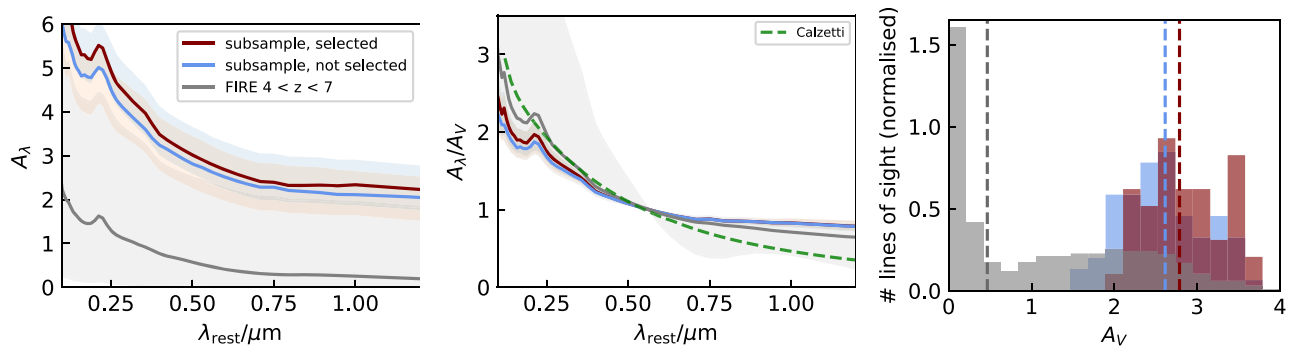

Figure 3. Left: dust attenuation curves for our subsamples of selected and not-selected sight lines (red and blue) of HST-dark sources, compared to those of all FIRE-2 snapshots at $4 < z < 7$ (gray). Solid lines and shaded regions show median curves and 1σ range for all lines of sight that fall into a given subsample, respectively. Center: dust attenuation curves as in the left panel, now normalized by A_V. We overplot the canonical Calzetti et al. (2000) law. In both panels, the average attenuation curves of selected and not-selected lines of sight are similar, with the median not-selected curve lying below the selected curve by $\Delta A_V < 0.22$ at all wavelengths. Right: the distribution of A_V values for each of the samples, with dashed lines showing medians (median $A_V = 2.8$, 2.6 for selected and not-selected orientations, respectively, compared to $A_V = 0.5$ for the whole FIRE sample at $z = 4$–7). Snapshots that are selected as HST-dark along one or more lines of sight are distinguished from the overall population by particularly high A_V values.

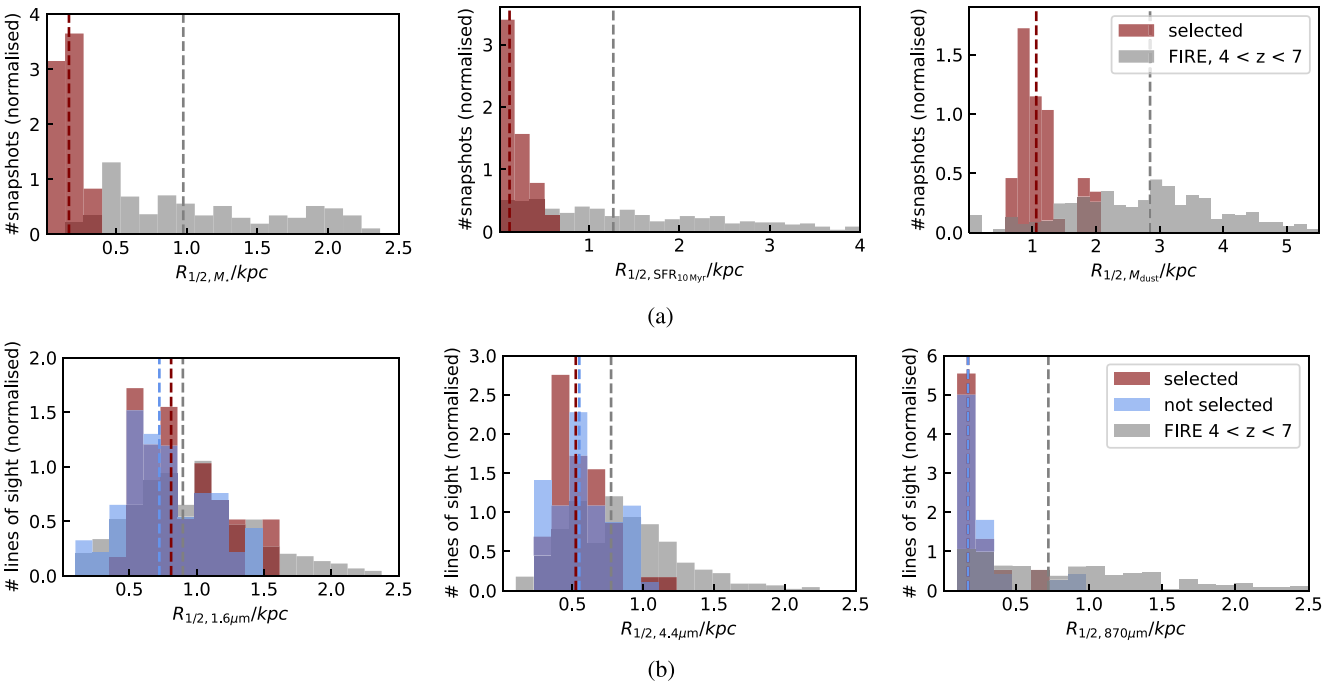

Figure 4. Physical (top panels) and observable (bottom panels) radii of HST-dark galaxies compared to all FIRE snapshots within a similar redshift range. (a) Distributions of radii containing half the stellar mass (left), SFR over the last 10 Myr (middle), and dust mass (right), for sources with HST-dark sight lines (red) compared to all FIRE-2 snapshots in the redshift range $4 < z < 7$ (gray). Snapshots with HST-dark sight lines display extremely compact stellar mass, star formation ($R_{1/2,M_*}$ & $R_{1/2,SFR} < 0.5$ kpc), and dust mass ($R_{1/2,M_{dust}} \sim 1$ kpc), compared to other snapshots at similar redshifts. (b) Distributions of half-light sizes at observed-frame 1.6 μm (left), 4.4 μm (middle), and 870 μm (right) for subsamples of selected and not-selected sight lines (red and blue), compared to those of all FIRE-2 snapshots at $4 < z < 7$ (gray). Differences in the distributions of half-light radii of selected and not-selected sight lines of snapshots with HST-dark sight lines are minor. HST-dark snapshots typically display more compact half-light radii than others at the same redshift at all three wavelengths, with the largest difference at 870 μm. The half-light sizes (at 1.6 and 4.4 μm) of HST-dark snapshots and the general population are more similar than the half-mass and half-SFR radii. This is because, for the more highly attenuated sources, more of the 1.6 and 4.4 μm emission is biased to larger radii due to central dust obscuration.

more extended dust mass distribution. This drives large optical depths.

3.3.2. Multiwavelength Sizes of HST-dark Sources

In Figure 4(b), we show histograms of half-light radii at 1.6, 4.4, and 870 μm, for selected and not-selected subsamples, as well as for all snapshots in the redshift range $4 < z < 7$. Note that these half-light sizes are calculated using a curve-of-growth technique, rather than from Sérsic profile fits to point-spread function–convolved images (as was performed in Parsotan et al. 2021 and Cochrane et al. 2023a). It is immediately clear that both selected and not-selected lines of sight of HST-dark snapshots are more compact, on average, than other simulated snapshots within the same redshift range. At 1.6 μm, median half-light radii are 0.81 and 0.72 kpc for selected and not-selected lines of sight, respectively, compared to 0.90 kpc for the whole $4 < z < 7$ sample. At 4.4 μm, median half-light radii are 0.52 and 0.55 kpc for selected and not-selected lines of sight,

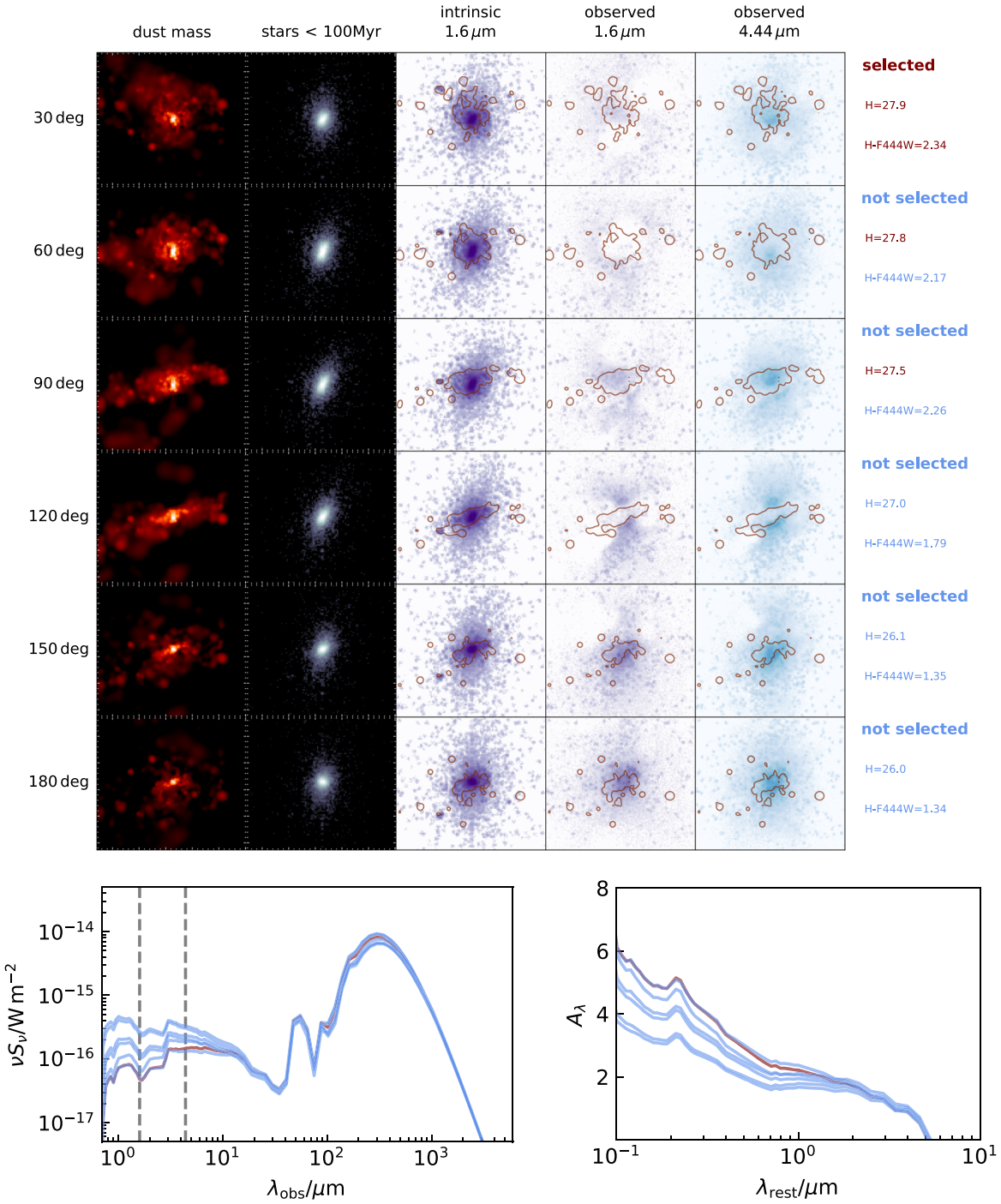

Figure 5. Top panels: projected distributions of dust mass, young stars, and predicted emission (intrinsic and observed) along different lines of sight for galaxy C1 at $z = 6.5$. Bottom panels: SED and attenuation curve for the different lines of sight. Vertical dashed lines indicate H band and 4.4 μm. Only one of the simulated lines of sight meets both H-band and color selection criteria of HST-dark galaxies. Two others meet the H-band criterion but not the color criterion. Along other lines of sight, the dust does not cover the young stellar emission as completely; hence, they appear brighter in the H band and are also too blue.

respectively, compared to 0.77 kpc for the whole $4 < z < 7$ sample. The compact sizes of our simulated sources are in line with recent observations: Gómez-Guijarro et al. (2023) found that the F444W-derived effective radii of optically dark/faint galaxies are 30% smaller than the average star-forming galaxy, at fixed stellar mass and redshift, with most $\lesssim$1.2 kpc. The difference between the spatial extent of the 4.4 and 1.6 μm emission is greatest for the HST-dark snapshots; this is driven by preferential dust attenuation in the inner regions of the galaxy affecting shorter wavelength light most strongly (see Cochrane et al. 2023a) and is in qualitative agreement with the recent observational study of Suess et al. (2022).

The most significant differences in size are seen at longer wavelengths. At 870 μm, median half-light radii are 0.17 kpc for both selected and not-selected lines of sight, compared to 0.72 kpc for the whole $4 < z < 7$ sample. The particularly compact dust continuum emission of observed K-dark SMGs was also noted by Smail et al. (2021). In our simulations, the compact emission is not only driven by a compact dust mass distribution (see Figure 4(a), right panel) but by particularly

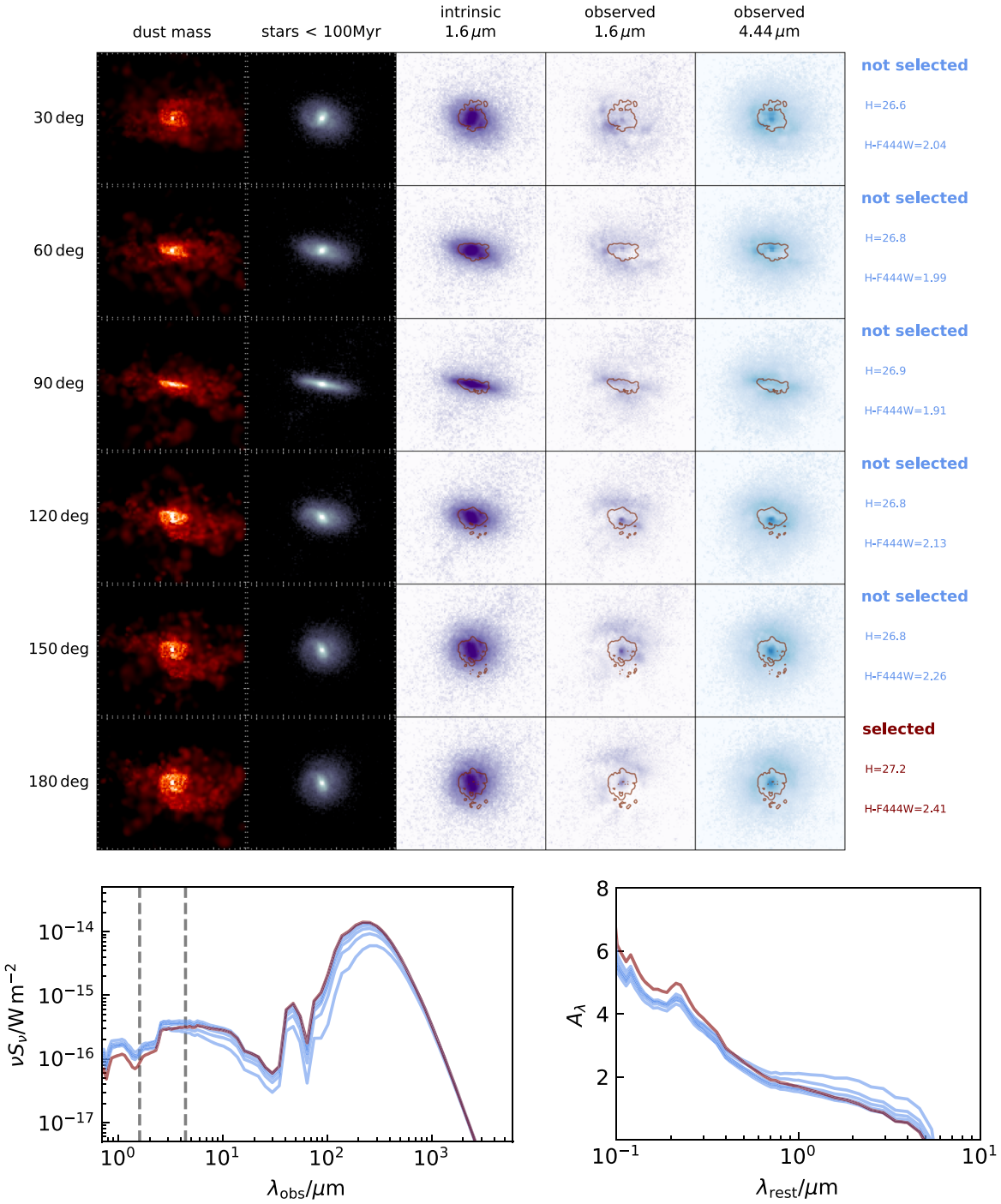

Figure 6. The same as Figure 5, but for galaxy B2 at $z = 5.4$. Only one line of sight meets the HST-dark criteria; the others are brighter in H and hence too blue.

compact star formation (see Figure 4(a), middle panel; this effect was also discussed in Cochrane et al. 2019, who showed that compact dust emission is driven by steep dust temperature gradients associated with compact star formation).

3.4. Understanding the Orientation Dependence of HST-dark Source Selection

In Section 2.3, we noted that for a given simulated galaxy snapshot, there exist lines of sight that meet the H-band magnitude and color criteria and others that do not. To illustrate this, in Figures 5 and 6 we show two examples of snapshots selected as HST-dark along just one of the modeled lines of sight. We plot projected dust mass, recently formed stars (with age <100 Myr), and predicted emission maps at observed-frame 1.6 and 4.4 μm. Contours of the projected dust mass are shown on both emission maps. We also show predicted SEDs and dust attenuation curves for all lines of sight.

Figure 5 shows galaxy C1 at $z = 6.5$. This galaxy is faintest in the observed-frame H band in the approximately face-on orientation (top panels). This is the only orientation for which both criteria are met. Viewing the galaxy from other angles (subsequent panels), the dust is less well oriented to cover the emission from the young stars; hence, the galaxy becomes brighter in H, which also leads to a bluer $H - \mathrm{F444W}$ color.

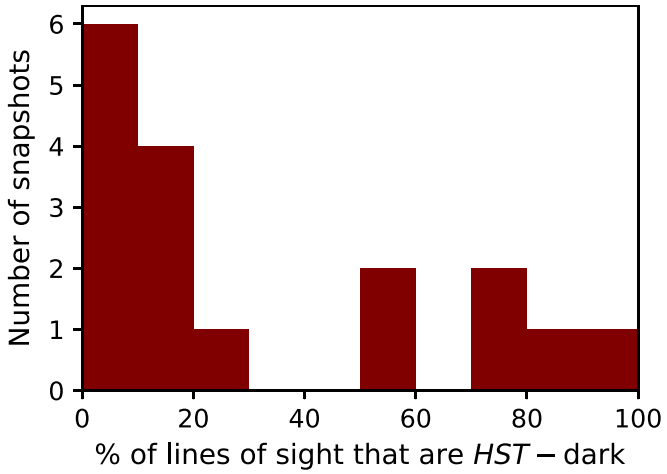

Figure 7. We reran the radiative transfer procedure for each snapshot with one or more previously identified HST-dark lines of sight. We used 50 lines of sight, evenly sampling solid angle. Here, we show the distribution of the percentage of snapshots that meet the HST-dark selection criteria. This ranges from 2% to 90%.

Figure 6 shows galaxy B2 at $z = 5.4$. This galaxy meets the criteria along just one of the modeled lines of sight; from all others, the galaxy appears too bright in H and also too blue. In both examples, there are lines of sight from which the H-band emission appears to escape from the edges of the dust distribution. This is in line with observations of dusty high-redshift galaxies (e.g., Hodge et al. 2016; Cochrane et al. 2021).

3.5. Implications of Line-of-sight Variations for Comparison with Models

One key result of this paper is the clear dependence of HST-dark source selection on line of sight. Only 1 of the 17 selected HST-dark galaxies is selected from all seven modeled orientations; the rest are selected along some lines of sight but not along others. To investigate this further, we repeat the radiative transfer calculation for each of the 17 selected snapshots, this time modeling 50 lines of sight, with solid angle evenly sampled. The number of lines of sight meeting the HST-dark selection criteria ranges from 1 to 45 (see Figure 7). In total, 268 of 850 modeled sight lines meet the criteria (32%). This has implications for the measurement of number densities of HST-dark sources from observations: for each galaxy selected as HST-dark, there are, on average, two others with the same physical properties that would not meet the selection criteria, simply because of sky orientation. More massive, submillimeter-bright sources, not simulated here, may be obscured along more lines of sight.

The high resolution of the FIRE simulations is key in enabling this result. In coarser resolution simulations, resolving the detailed geometry of gas and stars might not be possible. For example, the baryonic particle resolution of IllustrisTNG-100 is ∼40 times lower than our highest resolution simulations (Pillepich et al. 2018), and that of SIMBA's largest box is ∼14 times lower (Davé et al. 2019). Furthermore, simulations that do not explicitly resolve stellar feedback (e.g., using effective equation of state models) like IllustrisTNG will artificially suppress small-scale interstellar medium (ISM) clumping.

Semianalytic models tend to model galaxy geometry in a simplified manner. For example, Wang et al. (2019) compared the relative contributions of observed H-dropouts and modeled H-dropouts in the L-GALAXIES SAM (2015 version; Henriques et al. 2015) to the cosmic SFRD. However, the SAM models stars only as bulge, disk, and intracluster light components. Optical depths are calculated separately for the diffuse ISM and molecular birth clouds, following De Lucia & Blaizot (2007). The overall extinction curve is derived by assuming an "inclined slab" geometry implementation for the diffuse ISM. Although some geometric effects will be included as a result of the inclination angle, this is a simplistic implementation that does not allow for a clumpy ISM (or scattering into the line of sight). We caution that coarse-resolution hydrodynamical simulations and semianalytic models may not resolve the crucial dust–star geometry sufficiently for robust comparisons with observed HST-dark populations.

4. Conclusions

Using highly resolved zoom-in simulations from the FIRE suite, we perform the first detailed modeling of HST-dark galaxies, a population of galaxies identified observationally by their faint H-band magnitudes and red $H - \mathrm{F444W}$ colors. The high resolution of these simulations enables us to infer realistic distributions of dust and stars for galaxies spanning a range of stellar masses and redshifts. We run radiative transfer calculations on eight massive galaxies across $1 \lesssim z \lesssim 8$, and make predictions for the observed-frame UV–FIR emission. Applying selection criteria identical to those used in observational searches for IRAC/JWST-bright HST-dark galaxies, we naturally recover 17 galaxy snapshots that meet HST-dark selection criteria at one or more viewing angles, all in the redshift range $z = 4$–7. The four most massive halos all pass through an HST-dark stage at some point in their evolution. This is because those halos build enough stellar and dust mass early enough to meet the color selection. We then study the physical properties of these galaxies in light of the selections applied. Galaxy snapshots selected as HST-dark show high levels of dust attenuation ($2 < A_V < 4$) compared to others in the same redshift range. Physically, these high A_V values are associated with substantial dust masses ($M_{\mathrm{dust}} > 5 \times 10^6\, M_\odot$) and compact star formation ($R_{\mathrm{SFR\ 10\ Myr}} \sim 0.1$ kpc). Modeling the observable emission along additional lines of sight for each snapshot enables us to test the role of geometry in HST-dark galaxy selection. Importantly, galaxies that are HST-dark along some sight lines do not meet the criteria along others. We infer that the observational selection of HST-dark galaxies is subject to a strong viewing angle dependence: rather than a particularly special population, HST-dark galaxies are a subset of high-redshift galaxies viewed along lines of sight with particularly high dust attenuation. This result has implications for comparisons of observations with semianalytic models and coarse-resolution simulations that do not resolve the detailed geometry of stars and dust.

Acknowledgments

We thank the anonymous reviewer for helpful suggestions on an early version of this paper. The Flatiron Institute is supported by the Simons Foundation. The simulations presented in this work were run on the Flatiron Institute's research computing facilities (Gordon-Simons, Popeye, and Iron compute clusters), supported by the Simons Foundation. D.A.A. acknowledges support by NSF grants AST-2009687

and AST-2108944, CXO grant TM2-23006X, Simons Foundation Award CCA-1018464, and Cottrell Scholar Award CS-CSA-2023-028 by the Research Corporation for Science Advancement. F.C. acknowledges support from a UKRI Frontier Research Guarantee grant (PI: Cullen; grant reference EP/X021025/1).

Data Availability

The FIRE-2 simulations are publicly available (Wetzel et al. 2023) at http://flathub.flatironinstitute.org/fire. Additional FIRE simulation data are available at https://fire.northwestern.edu/data. A public version of the GIZMO code is available at http://www.tapir.caltech.edu/~phopkins/Site/GIZMO.html.

ORCID iDs

R. K. Cochrane https://orcid.org/0000-0001-8855-6107
D. Anglés-Alcázar https://orcid.org/0000-0001-5769-4945
F. Cullen https://orcid.org/0000-0002-3736-476X
C. C. Hayward https://orcid.org/0000-0003-4073-3236

References

Anglés-Alcázar, D., Faucher-Giguère, C. A., Quataert, E., et al. 2017, MNRAS, 472, L109
Baes, M., Verstappen, J., De Looze, I., et al. 2011, ApJS, 196, 22
Barrufet, L., Oesch, P. A., Weibel, A., et al. 2023, MNRAS, 522, 449
Behiri, M., Talia, M., Cimatti, A., et al. 2023, ApJ, 957, 63
Bertoldi, F., Carilli, C. L., Menten, K. M., et al. 2000, A&A, 360, 92
Bruzual, G., & Charlot, S. 2003, MNRAS, 344, 1000
Calzetti, D., Armus, L., Bohlin, R., et al. 2000, ApJ, 533, 682
Camps, P., & Baes, M. 2015, A&C, 9, 20
Caputi, K. I., Dunlop, J. S., McLure, R. J., et al. 2012, ApJL, 750, 1
Casey, C. M., Zavala, J. A., Manning, S. M., et al. 2021, ApJ, 923, 215
Cimatti, A., Andreani, P., Röttgering, H., & Tilanus, R. 1998, Natur, 392, 895
Cochrane, R. K., Anglés-Alcázar, D., Mercedes-Feliz, J., et al. 2023a, MNRAS, 523, 2409
Cochrane, R. K., Best, P. N., Smail, I., et al. 2021, MNRAS, 503, 2622
Cochrane, R. K., Hayward, C. C., Anglés-Alcázar, D., et al. 2019, MNRAS, 488, 1779
Cochrane, R. K., Hayward, C. C., & Anglés-Alcazar, D. 2022, ApJL, 939, L27
Cochrane, R. K., Hayward, C. C., Anglés-Alcazar, D., & Somerville, R. S. 2023b, MNRAS, 518, 5522
Cowie, L. L., Barger, A. J., Wang, W. H., & Williams, J. P. 2009, ApJ, 697, 1
Dannerbauer, H., Lehnert, M. D., Lutz, D., et al. 2002, ApJ, 573, 473
Davé, R., Anglés-Alcázar, D., Narayanan, D., et al. 2019, MNRAS, 486, 2827
De Lucia, G., & Blaizot, J. 2007, MNRAS, 375, 2
Dey, A., Graham, J. R., Ivison, R. J., et al. 1999, ApJ, 519, 610
Draine, B. T., & Salpeter, E. E. 1979, ApJ, 231, 77
Dudzevičiūtė, U., Smail, I., Swinbank, A. M., et al. 2020, MNRAS, 494, 3828
Dunlop, J. S., Cirasuolo, M., & McLure, R. J. 2007, MNRAS, 376, 1054
Dwek, E. 1998, ApJ, 1, 643
Elston, R., Rieke, G. H., & Rieke, M. J. 1988, ApJL, 331, L77
Enia, A., Talia, M., Pozzi, F., et al. 2022, ApJ, 927, 204
Fazio, G. G., Hora, J. L., Allen, L. E., et al. 2004, ApJS, 154, 10
Feldmann, R., Hopkins, P. F., Quataert, E., Faucher-Giguère, C. A., & Kereš, D. 2016, MNRAS, 458, L14
Feldmann, R., Quataert, E., Hopkins, P. F., Faucher-Giguére, C. A., & Kereš, D. 2017, MNRAS, 470, 1050
Finkelstein, S. L., Bagley, M., Song, M., et al. 2022, ApJ, 928, 52
Franco, M., Elbaz, D., Béthermin, M., et al. 2018, A&A, 620, A152
Frayer, D. T., Reddy, N. A., Armus, L., et al. 2004, AJ, 127, 728
Frayer, D. T., Smail, I., Ivison, R. J., & Scoville, N. Z. 2000, AJ, 120, 1668
Fujimoto, S., Bezanson, R., Labbe, I., et al. 2023, arXiv:2309.07834
Gómez-Guijarro, C., Magnelli, B., Elbaz, D., et al. 2023, A&A, 677, 1
Groves, B., Dopita, M. A., Sutherland, R. S., et al. 2008, ApJS, 176, 438
Henriques, B. M. B., White, S. D. M., Thomas, P. A., et al. 2015, MNRAS, 451, 2663
Hodge, J. A., Karim, A., Smail, I., et al. 2013, ApJ, 768, 91
Hodge, J. A., Swinbank, A. M., Simpson, J. M., et al. 2016, ApJ, 833, 103
Hopkins, P. F. 2015, MNRAS, 450, 53
Hopkins, P. F., Kereš, D., Oñorbe, J., et al. 2014, MNRAS, 445, 581
Hopkins, P. F., Narayanan, D., & Murray, N. 2013, MNRAS, 432, 2647
Hopkins, P. F., Wetzel, A., Keres, D., et al. 2018, MNRAS, 480, 800
Hopkins, P. F., Wetzel, A., Wheeler, C., et al. 2023, MNRAS, 519, 3154
Hu, E. M., & Ridgway, S. E. 1994, AJ, 107, 4
Huang, J. S., Zheng, X. Z., Rigopoulou, D., et al. 2011, ApJL, 742, 13
Hughes, D. H., Serjeant, S., Dunlop, J., et al. 1998, Natur, 394, 241
James, A., Dunne, L., Eales, S., & Edmunds, M. G. 2002, MNRAS, 335, 753
Karim, A., Swinbank, A. M., Hodge, J. A., et al. 2013, MNRAS, 432, 2
Kondapally, R., Best, P. N., Hardcastle, M. J., et al. 2021, A&A, 648, A3
Leitherer, C., Schaerer, D., Goldader, J. D., et al. 1999, ApJS, 123, 3
Liang, L., Feldmann, R., Hayward, C. C., et al. 2021, MNRAS, 502, 3210
Lilly, S., Eales, S. A., Gear, W. K., et al. 1999, ApJ, 518, 614
Ma, X., Hayward, C. C., Casey, C. M., et al. 2019, MNRAS, 487, 1844
Manning, S. M., Casey, C. M., Zavala, J. A., et al. 2022, ApJ, 925, 23
Nelson, E. J., Suess, K. A., Bezanson, R. S., et al. 2023, ApJL, 948, L18
Parsotan, T., Cochrane, R. K., Hayward, C. C., et al. 2021, MNRAS, 501, 1591
Pérez-González, P. G., Barro, G., Annunziatella, M., et al. 2023, ApJL, 946, L16
Pillepich, A., Nelson, D., Hernquist, L., et al. 2018, MNRAS, 475, 648
Rémy-Ruyer, A., Madden, S. C., Galliano, F., et al. 2014, A&A, 563, 31
Rodighiero, G., Bisigello, L., Iani, E., et al. 2023, MNRAS, 518, L19
Simpson, J. M., Smail, I., Dudzevičiūtė, U., et al. 2020, MNRAS, 495, 3409
Simpson, J. M., Smail, I., Swinbank, A. M., et al. 2015, ApJ, 799, 81
Simpson, J. M., Smail, I., Swinbank, A. M., et al. 2017a, ApJ, 839, 58
Simpson, J. M., Smail, I., Wang, W.-H., Riechers, D., & Dunlop, J. S. 2017b, ApJL, 844, L10
Simpson, J. M., Swinbank, A. M., Smail, I., et al. 2014, ApJ, 788, 125
Smail, I., Chapman, S. C., Blain, A. W., & Ivison, R. J. 2004, ApJ, 617, 64
Smail, I., Dudzeviciute, U., Gurwell, M., et al. 2023, ApJ, 958, 36
Smail, I., Dudzevičiūtė, U., Stach, S. M., et al. 2021, MNRAS, 502, 3426
Smail, I., Ivison, R., Blain, A., & Kneib, J.-P. 2002a, MNRAS, 331, 495
Smail, I., Ivison, R., Owen, F. N., Blain, A. W., & Kneib, J.-P. 2000, ApJ, 528, 612
Smail, I., Ivison, R. J., Kneib, J. P., et al. 1999, MNRAS, 308, 1061
Smail, I., Owen, F. N., Morrison, G. E., et al. 2002b, ApJ, 581, 844
Springel, V., White, S. D. M., Jenkins, A., et al. 2005, Natur, 435, 629
Stach, S. M., Dudzevičiūtė, U., Smail, I., et al. 2019, MNRAS, 487, 4648
Stach, S. M., Smail, I., Swinbank, A. M., et al. 2018, ApJ, 860, 161
Suess, K. A., Bezanson, R., Nelson, E. J., et al. 2022, ApJL, 937, L33
Sun, F., Egami, E., Pérez-González, P. G., et al. 2021, ApJ, 922, 114
Talia, M., Cimatti, A., Giulietti, M., et al. 2021, ApJ, 909, 23
Tielens, A. G. G. M., McKee, C. F., Seab, C. G., & Hollenbach, D. J. 1994, ApJ, 431, 321
van der Vlugt, D., Hodge, J. A., Algera, H. S. B., et al. 2022, ApJ, 941, 10
Walter, F., Decarli, R., Carilli, C., et al. 2012, Natur, 486, 233
Wang, T., Elbaz, D., Schreiber, C., et al. 2016, ApJ, 816, 84
Wang, T., Schreiber, C., Elbaz, D., et al. 2019, Natur, 572, 211
Wang, W.-H., Cowie, L. L., van Saders, J., Barger, A. J., & Williams, J. P. 2007, ApJL, 670, L89
Weingartner, J. C., & Draine, B. T. 2001, ApJ, 548, 296
Wetzel, A., Hayward, C. C., Sanderson, R. E., et al. 2023, ApJS, 265, 44
Williams, C. C., Labbe, I., Spilker, J., et al. 2019, ApJ, 884, 154
Wilson, G., Huang, J., PerezGonzalez, P. G., et al. 2004, ApJS, 154, 107
Xiao, M., Oesch, P., Elbaz, D., et al. 2023, arXiv:2309.02492
Yamaguchi, Y., Kohno, K., Hatsukade, B., et al. 2019, ApJ, 878, 73